

Evaluation and Modeling of Image Sharpness of Chinese Gaofen-1/2/6/7 Optical Remote-Sensing Satellites Over Time

Jiayang Cao, Litao Li , Yonghua Jiang , Xin Shen , Deren Li, and Meilin Tan

I. INTRODUCTION

Abstract—Image sharpness assesses detail visibility in remote-sensing images and measures sensors' details resolution capability. Sensor aging and environmental changes can degrade image sharpness and quality. The Gaofen (GF) satellites provide diverse remote-sensing imagery, but evaluations of their sharpness are limited. In this study, for the GF1/2/6/7 optical remote-sensing satellites in the space-based system of the China High-Resolution Earth Observation System (CHEOS) major special project, we evaluated the relative edge response (RER), full width at half maximum (FWHM), and modulation transfer function (MTF) of the images, using nearly ten years of ground target image data. This measures image sharpness and models how it changes over time with different sensors. Within ten years of on-orbit operation, the RER and MTF (@Nyquist frequency) of GF1/2 are 0.51 and 0.50, and 0.15 and 0.11, respectively. This indicated good image edge and high-frequency detail responsiveness, with FWHM of 1.16 and 1.17, respectively, showing a slight image sharpening. For GF6, the RER, MTF (@Nyquist frequency), and FWHM were 0.42, 0.09, and 1.39, indicating improved sharpening compared with GF1/2 but decreased edge and high-frequency detail response. The RER, MTF (@Nyquist frequency), and FWHM of the panchromatic images of GF7 were 0.32, 0.04, and 1.91, which indicate image blur. Meanwhile, the corresponding indicators for the multispectral images were 0.45, 0.14, and 1.40, better than the panchromatic images. Long-term data showed periodic sharpness variations in satellite images, with GF6s stability and minimal track differences being superior. The dynamic change pattern corresponds to a fourth-order polynomial model.

Index Terms—Full width at half maximum (FWHM), Gaofen (GF) remote-sensing satellites, image sharpness, modulation transfer function (MTF), relative edge response (RER).

Received 11 August 2024; revised 23 October 2024; accepted 31 October 2024. Date of publication 1 November 2024; date of current version 15 November 2024. This work was supported in part by the National Natural Science Foundation of China under Grant 42301439, and in part by the Hubei Provincial Natural Science Foundation of China under Grant 2023AFB450. (Corresponding author: Litao Li.)

Jiayang Cao and Litao Li are with the College of Urban and Environmental Sciences, Hubei Normal University, Huangshi 435002, China (e-mail: caojiaoyang@stu.hbnu.edu.cn; lilitao@whu.edu.cn).

Yonghua Jiang is with the School of Remote Sensing and Information Engineering, Wuhan University, Wuhan 430079, China (e-mail: jiangyh@whu.edu.cn).

Xin Shen and Deren Li are with the State Key Laboratory of Information Engineering in Surveying, Mapping, and Remote Sensing, Wuhan University, Wuhan 430079, China (e-mail: xinshen@whu.edu.cn; drli@whu.edu.cn).

Meilin Tan is with the Inner Mongolia Autonomous Region Surveying and Mapping Geographic Information Centre, Hohhot 010050, China (e-mail: tanmeilin@whu.edu.cn).

Digital Object Identifier 10.1109/JSTARS.2024.3490738

IN RECENT decades, the number and observation capabilities of global and regional Earth observation (EO) remote-sensing satellites have substantially increased. The increasing spatial resolution of these EO satellites has enabled them to identify tiny objects on the ground, such as road markings and man-hole covers, substantially enhancing the range of applications for remote-sensing imagery. However, the spatial resolution, that is, the minimum resolution of a remote-sensing sensor, is only one aspect of its spatial performance. At the same resolution, the detail-resolving capability of the sensor, embodied in the image as sharpness, is particularly important for accurately identifying and analyzing fine features, such as trees on both sides of the road and the edges of houses in Fig. 1.

Modulation transfer function (MTF), the frequency-domain manifestation of the point spread function (PSF), reveals the responsiveness of the imaging system to different spatial frequencies and characterizes the sharpness of ground features at different frequencies. MTF (@Nyquist frequency) has become one of the core metrics used by almost all remote-sensing satellites to measure the sensor performance and by many international agencies to evaluate image quality [1]. This is also the key metric recommended by the International Standards Organization for evaluating the sharpness of common images [2]. The full width at half maximum (FWHM) describes the width of the PSF in the spatial domain and is a pivotal metric for assessing the detail-resolving capability of high-resolution optical satellite imagery [3]. It is extensively used to evaluate image sharpness.

Meanwhile, relative edge response (RER) measures the responsiveness of the imaging system to feature edges [4], [5]. These constitute a comprehensive set of image sharpness assessment metrics from diverse perspectives, including frequency, spatial, and edge responses. This facilitates a more accurate understanding and assessment of the image quality.

Currently, various types of optical remote-sensing satellites use these three metrics, or one of them, to implement image sharpness assessments to monitor the quality of the sensor's imaging and image products. MTF has been employed for assessing image sharpness in optical remote-sensing satellites, such as AVNIR-2 [6], Terra [7], IKONOS [8], QuickBird [9], SPOT [10], and Landsat [11]. It is also a key indicator of sharpness in the image quality evaluation systems of some major

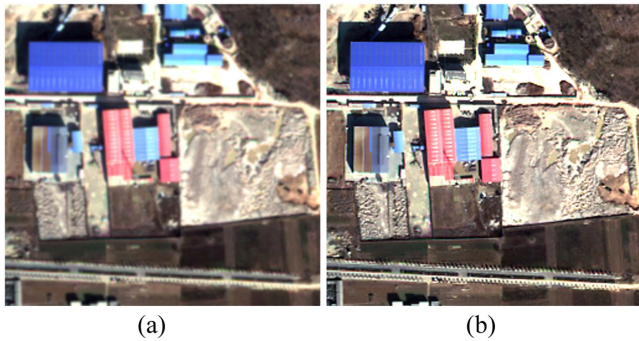


Fig. 1. Image sharpness comparison. (a) Image is blurry. (b) Image is in focus.

international agencies, such as the quality evaluation programs developed by ESA and NASA [12], [13], [14]. FWHM metrics in the spatial domain have been applied to high-resolution remote-sensing satellites, such as IKONOS [15], QuickBird [16], Pleiades 1A [17], WorldView-2 [18], GeoEye-1 [19], and others. Recently, to achieve consistency, accuracy, and comparability in assessing image sharpness, the simultaneous use of three metrics to combine analyzing image sharpness has been applied to satellites, such as Satellogic NewSat [20], Pléiades Neo [21], Landsat 8 OLI [22], and Landsat 9 TIRS-2 [23].

The Gaofen (GF) series of remote-sensing satellites, which are space-based systems for the China High-Resolution Earth Observation System (CHEOS), has been a crucial pillar of China's national EO capability since the launch of the first satellite in 2013. They deliver a variety of satellite remote-sensing imagery across diverse sectors. However, to date, relatively few studies have evaluated GF satellite sharpness. The sharpness of GF-4 images has been assessed using a single indicator [24]. Regarding the joint systematic assessment of multiple indicators, Li et al. [25] established a radiometric quality evaluation index system for GF remote-sensing imagery in China. This measured the radiometric quality level of GF satellite imagery products on a systematic basis over a longer timescale. However, this study measured the detail resolution of images using MTF, and the results were up to 2022.

In this study, we collected ground knife-edge target images from satellite launch to 2024 and used three sharpness evaluation indices, namely, RER, FWHM, and MTF. We aimed to evaluate the sharpness of the GF1/2/6/7 satellite images from different dimensions and examine the variation rule of the sharpness over time, providing a scientific basis for the on-orbit quality control of satellite images and laying the foundation for expanding the depth of the data application.

II. IMAGE SHARPNESS ESTIMATION METHOD

The RER, FWHM, and MTF can be obtained by processing the edge spread function (ESF). For example, the RER can be calculated directly from the ESF, the FWHM can be calculated from the line spread function (LSF) derived from the ESF, and the MTF can be obtained from the Fourier-transformed (FT) LSF. Targets with slanting edges have become the preferred

method for indirectly measuring the MTF from the ESF in high-resolution optical remote-sensing satellites because of their simple deployment, reliable accuracy, and easy identification from the image. Using this method, the edge subpixel position is extracted from the edge target remote-sensing image. The subpixel position is then aligned and encrypted to obtain the ESF, after which the Fourier transform is used to process the LSF to obtain the MTF. Therefore, these three metrics can be calculated directly based on the ground-based fixed-edge target. The results of the metrics in both the along-track (ALT) and cross-track (ACT) directions can be obtained simultaneously, as shown in Fig. 2.

A. Oversample ESF and LSF Calculation

All the calculations of the sharpness metrics rely on the acquisition of high-precision ESFs. ISO 12233-2023 recommends the use of Hann windows and high-order polynomial fitting to extract the subpixel locations of sharply curved edges [26]. However, in remote-sensing images, owing to ringing artifacts and noise at the straight edge, high-order polynomial fitting is easily oversensitive to these disturbances. This results in a fitting curve that does not accurately reflect the true edge. Most GF satellite image products have been processed by MTF compensation (MTFC), with more ringing artifacts. Meanwhile, certain edge targets, such as the John C. Stennis Space Center (JC) target in the United States, have had problems with noise effects during certain periods, as shown in Fig. 3.

Considering that the shape of the Boltzmann function is highly consistent with the step change of the edge and the subpixel center symmetry, it shows high robustness and stability in edge detection [25]. We used this function to fit the edges to extract subpixel locations to improve the accuracy and stability of the encrypted sampling ESF. Its function is expressed as follows:

$$y = \frac{A1 - A2}{1 + e^{\frac{x-x_0}{dx}}} + A2 \quad (1)$$

where $A1$, $A2$, x_0 , and dx are the parameters and the function is centrally symmetric about point $(x_0, \frac{A1+A2}{2})$. When $x \rightarrow +\infty$, $y = A2$ and $x \rightarrow -\infty$, $y = A1$. x_0 is the subpixel edge position.

The encrypted ESF can be differentiated to obtain the LSF. However, background dispersion and ringing artifacts exist in the ESF as the image edge response. This is the part that contains the true response of the sensor to the ground target imaging. If a filter is used for forced smoothing, feedback on the true response of the sensor may be lost. The center difference method is suitable for situations where it is difficult to directly calculate the difference or where the data contain noise. The center difference simultaneously considers the values of the function on both sides of a point. This reduces the truncation error and the error by taking the average of the two points. This helps to suppress the effect of noise and can provide higher accuracy than the forward or backward difference. Therefore, applying the center difference method to the LSF calculation can effectively mitigate

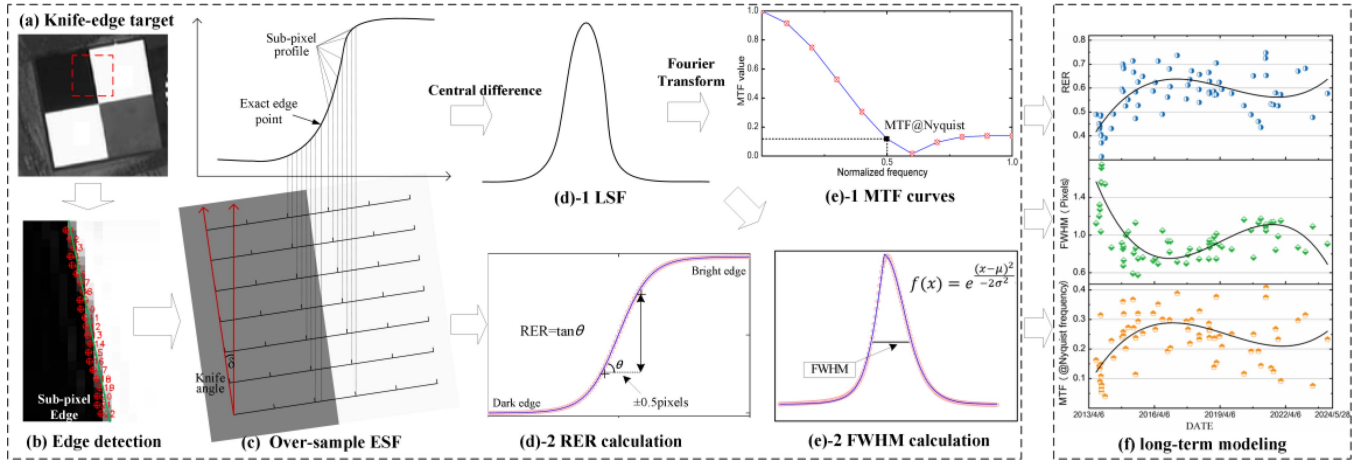


Fig. 2. Schematic diagram of image sharpness measurement process using slanted knife-edge target. (a) Knife-edge target. (b) Edge detection. (c) Oversample ESF. (d)-1 LSF. (d)-2 RER calculation. (e)-1 MTF curves. (e)-2 FWHM calculation. (f) Long-term modeling.

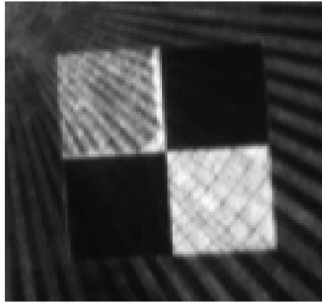


Fig. 3. JC target with noise (GF7).

ESF noise interference using the following equation:

$$f'(x) \approx \frac{f(x+h) - f(x-h)}{2h} \quad (2)$$

where $f'(x)$ is the derivative of the function at the point x , $f(x+h)$ is the value of the function at a distance h to the right of the point x , $f(x-h)$ is the value of the function at a distance h to the left of the point x , and h is the step size, that is, a small positive number, here set to 0.05.

B. RER, FWHM, and MTF Calculation

MTF values at Nyquist frequencies do not adequately capture MTF performance in the low-to-medium spatial frequency range. ESF-based RER is defined as the slope of the edge response within ± 0.5 pixels of the center of the edge. This indicates the change in contrast on a pixel in the midfrequency range of the imaging system response. The steeper the edge, the higher the RER value, indicating a sharper image. A lower RER value indicates a blurred image. The formula used is given as follows:

$$\text{RER} = \tan \theta \quad (3)$$

where θ is the angle of the edge response within ± 0.5 pixel of the center of the edge.

The LSF is a representation of the PSF in a 1-D case, which can describe the response of an imaging system to a linear object and is used to assess the sharpness of an image. The width of an LSF can be described by its FWHM, which measures width at half maximum (FWHM). When the LSF is described by a Gaussian function, its FWHM is calculated as follows [27]:

$$\text{FWHM} = 2\sigma\sqrt{2\ln 2} \quad (4)$$

where σ is the standard deviation (SD) of the Gaussian function.

The FWHM is closely related to image sharpness, with sharper images typically having a smaller FWHM. A smaller FWHM value indicates that the imaging system can capture finer ground details. However, when the FWHM is extremely small, it can lead to image oversharpening, pixelation, or aliasing, which can affect the overall image quality [28].

The FT LSF yielded the MTF, and the MTF value at the Nyquist frequency was selected to measure the sharpness and aliasing of the image.

C. Modeling Long Time Series

During the stability operation of remote-sensing satellites, the image data acquired by on-orbit imaging carry temporal attributes, and their sharpness indicators, such as RER, FWHM, and MTF, reflect the performance of the sensor at the imaging moment and accurately characterize the image sharpness. Owing to the vibration of the satellite platform and the uncertainty of the imaging medium, the performance of the sensor shows a nonlinear decay trend; additionally, up and down fluctuations occur with the adjustment of the sensor parameters, and these fluctuations do not have a clear regularity. Polynomial models can capture the trend from linear to nonlinear with different orders. Lower order polynomials are sufficient for describing simple linear or quadratic variations. Meanwhile, higher order polynomials are capable of modeling more complex nonlinear

TABLE I
SENSOR CONFIGURATIONS AND LAUNCH TIME FOR GF1/2/6/7

Parameter	Launch time	Sensor	Spatial resolution (m)	Swath width (km)	Revisit cycle (sidesway)
GF1	2013.4	2 PMS 4 WFV	PAN 2 MS 8 16	60 800	4 days
GF2	2014.8	2 PMS	PAN 0.8, MS 3.2	45	5 days
GF6	2018.6	1 PMS 1 WFV	PAN 2 MS 8 16	90 800	4 days
F7	2019.11	BWD FWD	PAN 0.65 MS 2.6 PAN 0.8	20	59 days

fluctuations and are suitable for describing complex changes in image sharpness over time. The polynomial fitting function is assumed to be

$$y(t) = a_k t^k + a_{k-1} t^{k-1} + \dots + a_2 t^2 + a_1 t + a_0 \quad (5)$$

where $y(t)$ is the predicted value at time point t , a_k, a_{k-1}, a_2, a_1 , and a_0 are the model parameters, and k is the order of the polynomial. The appropriate polynomial order k can be determined based on the time-series length to be analyzed, the number of samples, fitting accuracy, and interpretability.

III. ASSESSMENT SATELLITES AND DATA

A. GF Remote-Sensing Satellites

The GF1/2/6/7 satellites are a part of the CHEOS project, comprising four linear push-broom optical remote-sensing satellites. GF1 and GF6 provide networked observation capabilities and have panchromatic multispectral sensors (PMS) and wide field of view (WFV) sensors. PMS can provide panchromatic (PAN) and multispectral (MS) imagery. The GF2 is China's first submeter-resolution optical EO satellite, achieving a resolution of 0.8 m. GF7, a 3-D mapping satellite, was equipped with a 0.8-m forward-looking sensor (FWD), a 0.65-m backward-looking sensor (BWD), and a laser altimeter, which is used to realize 1:10 000 scale mapping. The launch dates and the main sensors of GF1, GF2, GF6, and GF7 are listed in Table I.

B. Edge Target Selection

Three different artificial knife targets were chosen to study the sharpness of the GF images. These artificial tilted edge targets are mainly based on the Baotou and Songshan radiometric calibration fields in China, supplemented by edge targets from JC in the USA. The key information for each edge target is presented in Table II. For edge selection, the ALT and ACT spatial performance of the sensor was evaluated using the edges of the adjacent high–low reflectivity target combinations. For ALT sharpness, the 2–3 edges of the JC and the 1–2 edges of Songshan and Baotou were used. ACT sharpness was assessed using Songshan's 2–3 edge, Baotou's 1–3 edge, and the JC 1–2 edge.

TABLE II
ARTIFICIAL EDGE TARGET INFORMATION


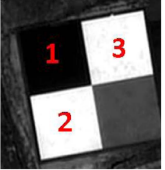
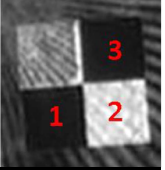
Name	Lat./Lon. (degree)	Size	Reflectance	Image example (GF2 PAN)
Songshan	34.53553/ 113.0957	35×35 m	5% at Zone 1/3, 60% at Zone 2	
Baotou	40.85169/ 109.6291	48×48 m	8% at Zone 1, 60% at Zone 2/3	
JC	30.38557/ 89.6285	25×25 m	5% at Zone 1/3, 20% at Zone 2	

TABLE III
EVALUATION SCENE INFORMATION

Time span	Satellite	Band	Cycles (month)	Average number of scenes in a single cycle (scene)
2013.6–2024.4	GF1	PAN	3	1.4
		PAN		1.6
2014.10–2023.9	GF2	PAN	6	1.7
		PAN		1.6
2018.9–2024.3	GF6	PAN	3	2
		PAN		3
2020.5–2023.8	GF7	MS	6	3
		PAN		3

C. Data Amount

A total of 295 valid target images with clean atmospheric conditions were acquired by four satellites and eight types of sensors for the evaluation experiments. This encompassed three months as a cycle for GF1 and GF6 and six months for GF2 and GF7. The specific number of imaging times is shown in Table III.

IV. RESULTS AND ANALYSIS

Image sharpness during ten years of on-orbit operation of the four-satellite eight-type sensors was evaluated on the long time-series data of visible light remote-sensing images of the GF1/2/6/7 satellites. By analyzing the RER, FWHM, and MTF (@Nyquist frequency), the quality and trend of variation in the image sharpness were determined to monitor the long-term stability of the imaging system.

A. Long Time-Series Polynomial Model Order Determination

When evaluating the long time-series sharpness of GF series remote-sensing images using a polynomial model to analyze its variation trend, the optimal order needs to be determined.

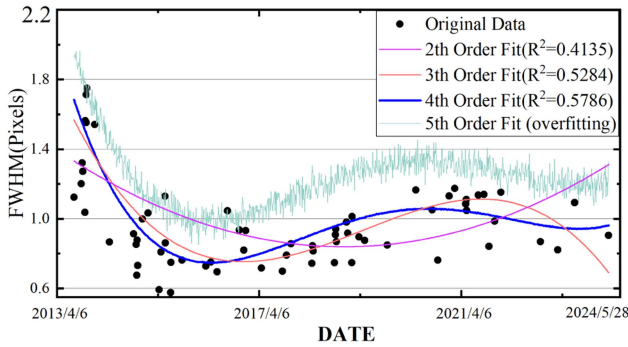


Fig. 4. Comparison of FWHM long time-series samples fitted with different polynomial orders for GF1 PMS.

Since the results of the sharpness assessment of each sensor are generally similar, the FWHM values of GF1 PMS sensor were chosen to determine the optimal order. As shown in Fig. 4, starting from the second-order polynomial, the R^2 fitting accuracy improved continuously with the increasing order, reaching 0.5786 for the fourth-order polynomial. However, using a fifth-order polynomial led to overfitting. Therefore, the fourth-order polynomial model was used to analyze the long time-series sharpness variation in this study.

B. Sharpness of Four GF Satellites and Its Variations

1) *GF1*: GF1 satellites' two sensors exhibited a wave-like trend of RER and MTF (@Nyquist frequency) in different directions, which were first elevated, then oscillated, and then decreased, as shown in Fig. 5(a), (b), (e), and (f). This is consistent with the performance degradation, optimization, and reoptimization measures that the satellites have undergone during on-orbit operation. The tendency of the FWHM was the opposite, as shown in Fig. 5(c) and (d). This indicates that system performance optimization leads to image refinement and FWHM reduction, followed by performance degradation leading to image blurring and FWHM increase. This is ultimately improved by performance compensation.

PMS1 and PMS2 sensors in the RER and MTF (@Nyquist frequency) values of ACT were generally larger than that of ALT (see Fig. 5). The specific relative deviations were in the order of 5.7%, 12.9%, 51.4%, and 53.8%. This indicates that the sharpness of ACT was better than that of ALT. In contrast, the FWHM values were smaller than those for the ALT, with relative deviations of 17.5% and 28.2%, respectively. The edge sharpness of ALT was slightly lower than that of ACT because of the motion blurring effect of ALT during sensor imaging.

In terms of the distribution of SDs, RER and MTF (@Nyquist frequency) had small SD, distributed between 0.10 and 0.04. This indicated that the magnitude of variation in these indicators was small and the consistency of the data was high. The SD of FWHM is larger and distributed between 0.45 and 0.26. This indicated that the magnitude of change in FWHM was larger and the consistency of the data was relatively low. The evaluation results showed that the imaging sharpness of the GF1 sensor did not vary markedly and exhibited high stability. The PMS1 sensor

of the GF1 satellite, whose ALT spatial sharpness assessment metrics had the smallest variation amplitude, showed a more stable performance [see Fig. 5(a), (c), and (e)].

2) *GF2*: GF2s satellites' sensors showed different wave-like trends in RER and MTF (@Nyquist frequency) in different directions, that is, ALT showed an increase and then stabilization. Meanwhile, ACT showed a slight fluctuation in the first period and a markedly decrease in the second three years of the evaluation cycle [see Fig. 6(a)–(f)]. Meanwhile, the FWHM trends in both tracks of the image showed a decrease, followed by an increase [see Fig. 6(c) and (d)]. Overall, these trends reveal the cyclic performance adjustment and management that a satellite sensor undergoes during in-orbit operation to maintain the stability and data quality of its imaging system during long-term operations.

The RER and MTF at the Nyquist frequency of PMS1 and PMS2 in the ACT were generally larger than those of the ALT (see Fig. 6), with specific relative deviations of 21.8%, 9.4%, 57%, and 54.1%, respectively. Meanwhile, the FWHM of ACT was smaller than that of ALT, with intersensor FWHM relative deviations of 38.1% and 15.5%. This indicates that the sharpness of the ACT image was better than that of the ALT image, which is consistent with the performance of GF1.

The distribution of SD, RER, and MTF (@Nyquist frequency) exhibited small SDs, distributed between 0.12 and 0.04, indicating that the magnitude of change in these indicators was small and the consistency of the data was high. In contrast, the SD of FWHM was larger, distributed between 0.29 and 0.25. The magnitude of change in FWHM was larger, with relatively lower consistency of the data. The evaluation results showed that the performance of the GF2 sensor did not change much and exhibited high stability. The stability of the sharpness evaluation was similar to that of the GF1 satellite.

3) *GF6*: The GF6 PMS RER, FWHM, and MTF (@Nyquist frequency) metrics all showed a smooth and slightly fluctuating trend in ALT. Meanwhile, ACT showed a slow increase in RER and MTF (@Nyquist frequency) fluctuations and a slow decrease in FWHM fluctuations [see Fig. 7(a)–(c)]. These results reflect the stable image ALT sharpness and improved imaging sharpness of ACT.

The ACT and ALT of the three indices [RER, FWHM, and MTF (@Nyquist frequency)] of the GF6 sharpness assessment were the same. The relative deviation was substantially lower than that of GF1 and GF2, at 3.2%, 8%, and 27.1%, respectively. This indicates that the sharpness of the images in different tracks was the same, but different from that of the GF1 and GF2 satellites. The sharpness assessment of the ACT of GF1 and GF2 was markedly better than that of ALT.

In the distribution of SD, RER and MTF (@Nyquist frequency) exhibited smaller SD, distributed between 0.05 and 0.03. Meanwhile, the SD of FWHM was 0.17–0.15. The evaluation results showed that the variation in sharpness indicators was better than that of GF1 and GF2, indicating that the GF6 satellite payload has high stability owing to the accumulation of technology in the manufacture of remote-sensing sensors and the enhancement of the image-shift compensation ability of the satellite platform operating ALT.

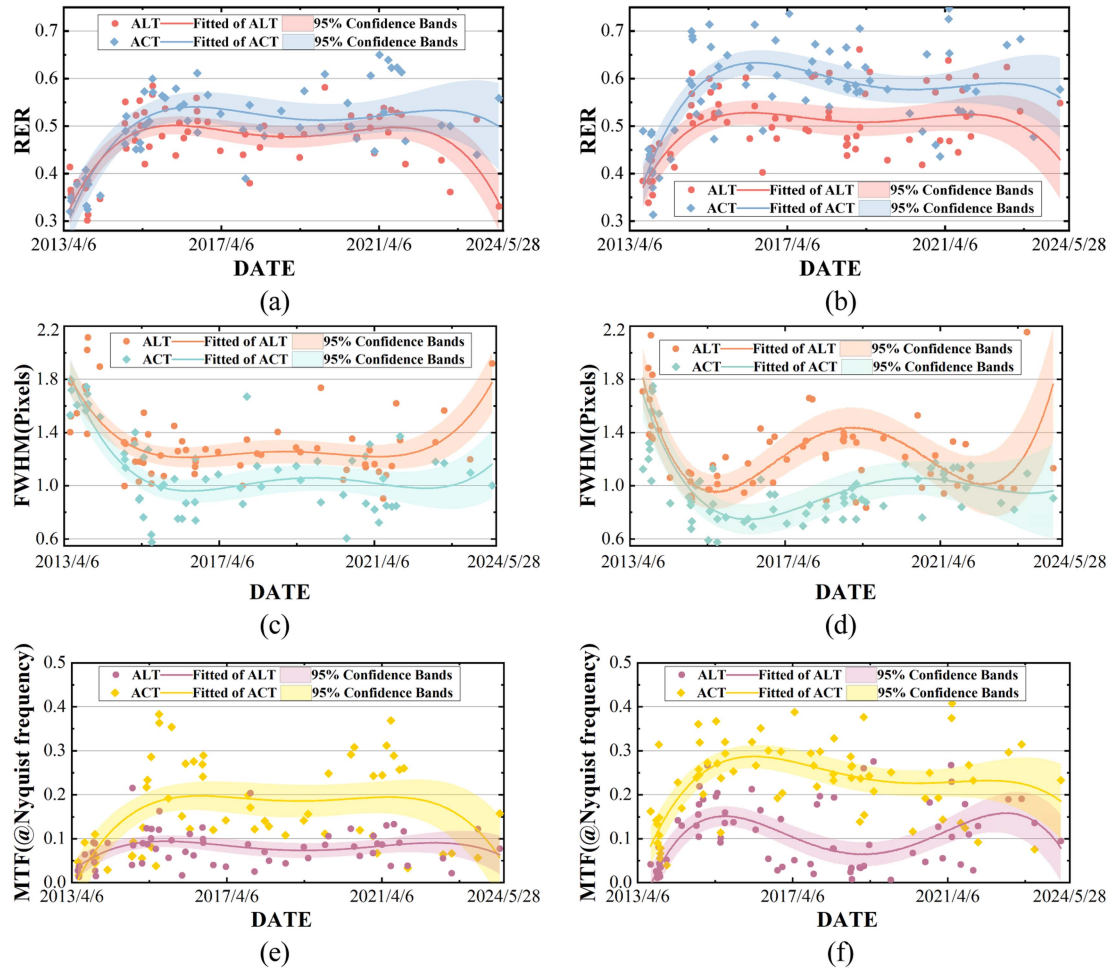


Fig. 5. GF1 image sharpness long time-series evaluation results. (a) RER of PMS1. (b) RER of PMS2. (c) FWHM of PMS1. (d) FWHM of PMS2. (e) MTF (@Nyquist frequency) of PMS1. (f) MTF (@Nyquist frequency) of PMS2.

4) *GF7*: As the GF7 satellite has been in orbit for a relatively short period, for just over three years in the assessment period, the trend has been upward and downward. BWD MS showed a slow rise in RER and MTF (@Nyquist frequency) in ALT. ACT showed a wave-like change of falling, then rising, and then falling [see Fig. 8(a) and (g)]. Meanwhile, the FWHM showed the opposite trend to RER in all directions [see Fig. 8(d)]. The RER and MTF (@Nyquist frequency) of the BWD-PAN both showed a slow decrease followed by a slight increase [see Fig. 8(b) and (h)]. The FWHM showed the opposite trend to the RER [see Fig. 8(e)]. The RER of FWD showed an overall decreasing trend [see Fig. 8(c)]. FWHM showed an increasing trend in ALT, and ACT exhibited a decrease followed by an increase [see Fig. 8(f)]. The MTF (@Nyquist frequency) showed slight fluctuations, but the result was stable in the evaluation cycle [see Fig. 8(i)]. Summing up the sharpness assessment results of each sensor, the FWD image exhibited poor sharpness results with a blurring effect. Meanwhile, the MS image of the BWD had good sharpness with better detail-capturing ability while maintaining high-edge sharpness.

The RER and MTF (@Nyquist frequency) of BWD-MUX, BWD-PAN, and FWD in ACT were generally larger than those

of ALT, with relative deviations of 11.6%, 8.9%, and 18.1%, and 25.7%, 18.5%, and 44.4%, respectively. Meanwhile, the FWHM of each ACT sensor was smaller than that of ALT, with relative deviations of 11.3%, 3.5%, and 23.8%, respectively. The image sharpness assessment of ACT was better than that of ALT and was most prominent in the FWD images.

In the distribution of the SD, the SD of the RER and MTF (@Nyquist frequency) was small, distributed between 0.12 and 0.04. Meanwhile, the SD of the FWHM was larger, distributed between 0.29 and 0.25, and the consistency of the data was relatively high. The assessment results showed that the performance of the GF7 sensor did not change markedly and exhibited good stability. The stability of the GF7 satellite image sharpness assessment was the same as that of the GF1 and GF2 images.

C. Five-Year Sharpness Assessment

The design lifetime of the GF series of satellites is 5–8 years [29]. Five years were considered a key time point to assess and analyze the changes in image sharpness during and after five years of satellite operation in orbit. According to the evaluation results, the image sharpness of these satellites was well maintained during the five-year evaluation period, as shown in

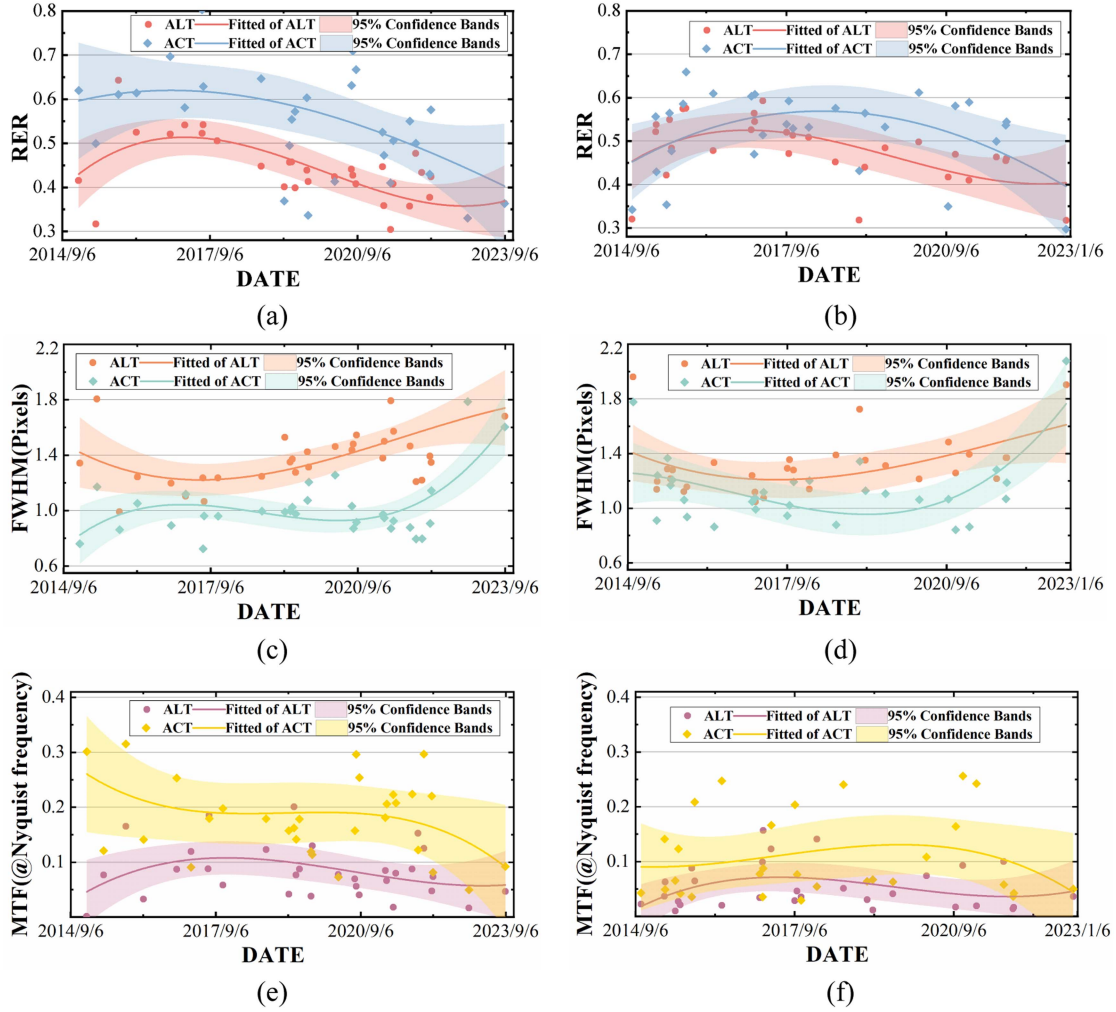


Fig. 6. GF2 image sharpness long time-series evaluation result. (a) RER of PMS1. (b) RER of PMS2. (c) FWHM of PMS1. (d) FWHM of PMS2. (e) MTF (@Nyquist frequency) of PMS1. (f) MTF (@Nyquist frequency) of PMS2.

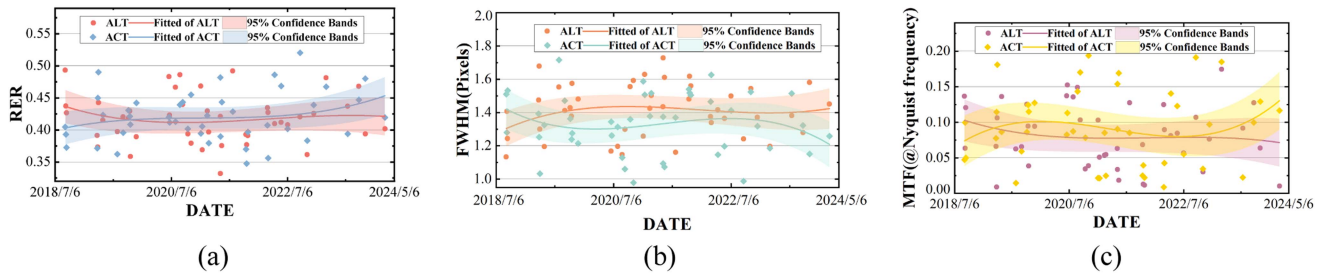


Fig. 7. GF6 PMS image sharpness long time-series evaluation results. (a) RER. (b) FWHM. (c) MTF (@Nyquist frequency).

Table IV. This indicates that the remote-sensing sensor payloads demonstrated high imaging performance and reliability during the robust period of the design lifetime, which met the requirements of the intended imaging missions. With measures, such as the MTF in place during on-orbit operations, the sharpness performance remained excellent even after five years, as shown in Table V. This also indicates that the satellite's maintenance and compensation measures have been implemented properly, effectively extending its service life and ensuring the continued provision of quality imagery.

V. DISCUSSION

Knife-edge subpixel detection, target background noise, and ringing artifacts at target edges pose challenges to the accuracy of the sharpness assessment results. In this section, the effectiveness of the Boltzmann function for subpixel edge-location detection and ESF center difference in calculating LSF antinoise and suppressing ringing artifacts are discussed and verified. The reliability of the assessment results was checked by comparing the sharpness results of the GF images in this study with other

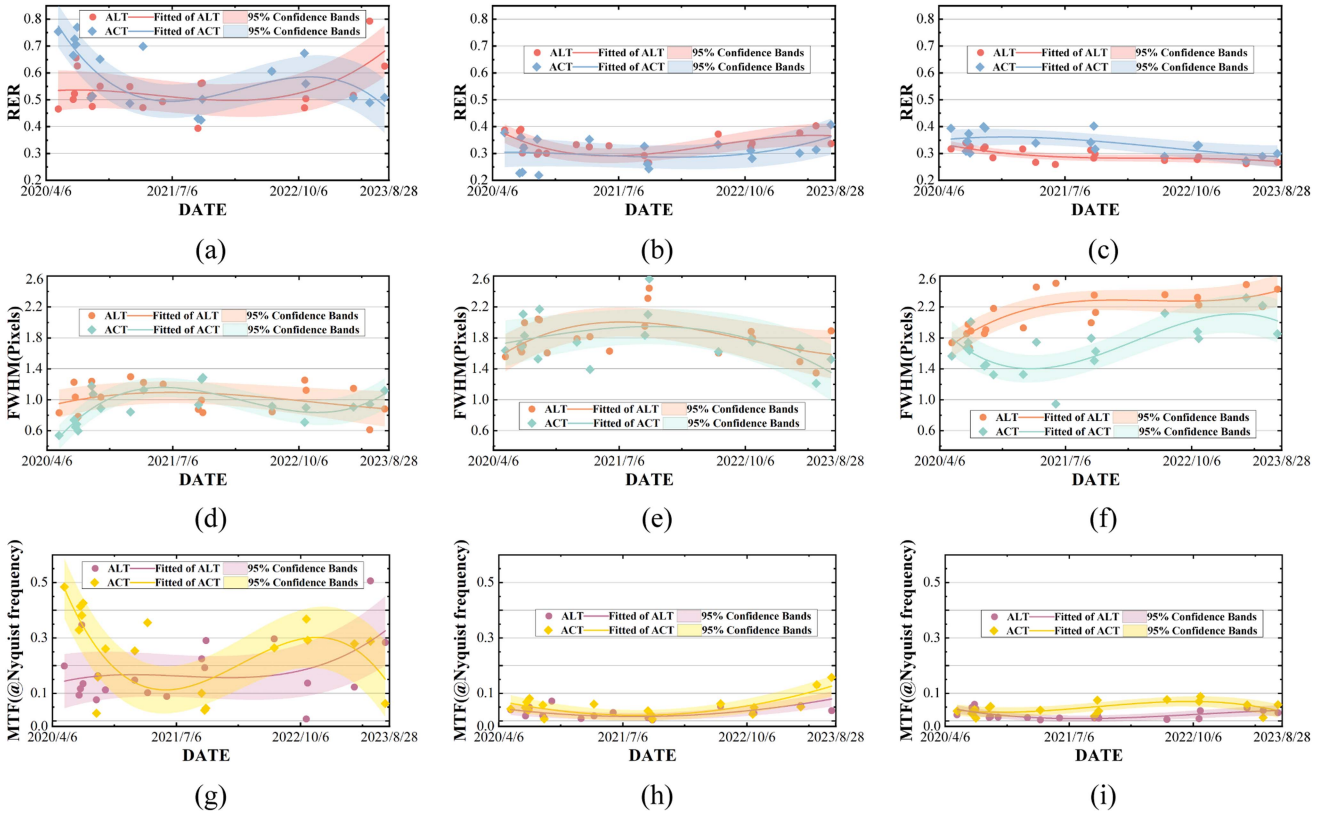


Fig. 8. GF7 image sharpness long time-series evaluation result. (a) RER of BWD MS. (b) RER of BWD-PAN. (c) RER of FWD PAN. (d) FWHM of BWD MS. (e) FWHM of BWD-PAN. (f) FWHM of FWD PAN. (g) MTF (@Nyquist frequency) of BWD MS. (h) MTF (@Nyquist frequency) of BWD-PAN. (i) MTF (@Nyquist frequency) of FWD PAN.

TABLE IV
AVERAGE IMAGE SHARPNESS METRICS OF SATELLITES IN ORBIT FOR FIVE YEARS

Satellite	Sensor	ACT			ALT		
		RER	FWHM/ pixels	MTF (@Nyquist frequency)	RER	FWHM/p ixels	MTF (@Nyquist frequency)
GF1	PMS1	0.4720	1.1942	0.1489	0.4572	1.3581	0.0788
	PMS2	0.5576	0.9798	0.2309	0.4894	1.2024	0.1075
GF2	PMS1	0.5849	0.9858	0.1940	0.4717	1.2957	0.0944
	PMS2	0.5271	1.1233	0.1009	0.4952	1.2863	0.0548
GF6	PMS	0.4180	1.3869	0.0901	0.4176	1.4053	0.0826
GF7	BWD-MUX	0.5998	0.8816	0.2713	0.5304	0.9816	0.2014
	BWD-PAN	0.3071	1.8343	0.0556	0.3345	1.8979	0.0342
	FWD	0.3619	1.7466	0.0456	0.2963	2.1615	0.0258

TABLE V
AVERAGE IMAGE SHARPNESS METRICS OF SATELLITES IN ORBIT AFTER FIVE YEARS

Satellite	Sensor	ACT			ALT		
		RER	FWHM/ pixels	MTF(@Nyquist frequency)	RER	FWHM/ pixels	MTF(@Nyquist frequency)
GF1	PMS1	0.5243	1.0205	0.1823	0.4825	1.2442	0.0822
	PMS2	0.5902	0.9075	0.2338	0.5108	1.2166	0.1073
GF2	PMS1	0.5208	1.0350	0.1749	0.3928	1.4955	0.0642
	PMS2	0.5012	1.1676	0.1197	0.4363	1.3602	0.0463
GF6	PMS	0.4489	1.2440	0.1152	0.4213	1.4369	0.0671

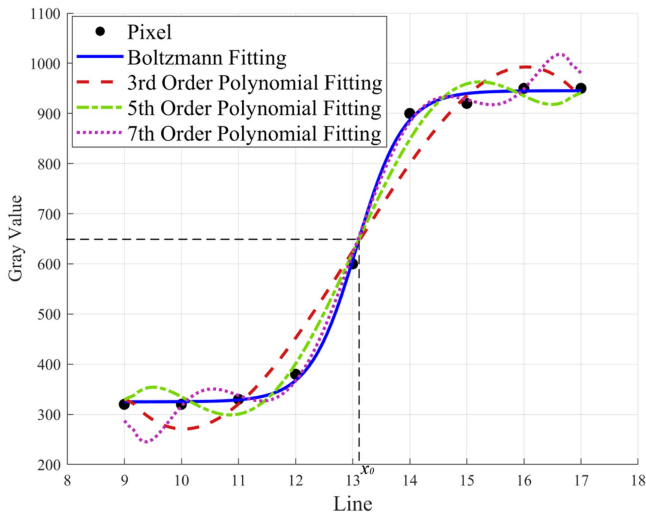


Fig. 9. Comparison of the fitting effects of the polynomial models with different orders and Boltzmann models.

research results in the existing literature. Finally, the effect of solar angle on sharpness assessment is also discussed.

A. Subpixel Edge-Location Detection

The characterization of artificial knife-edge targets has a higher and lower reflectance in both head and ends and is a little oversmooth in the middle. This property of the edge is in high agreement with the shape of the Boltzmann function. In comparison with the polynomial model, fitting the edge profile with the Boltzmann function achieves higher accuracy and more reliable stability with better noise robustness. An abnormal phenomenon where the subpixel locations appear unstable with an increase or decrease of sample points, relative to cubic polynomial fitting, will not occur. As shown in Fig. 9, the fitting results were bad and not ideal due to the volatile nature of low-order polynomial and the oscillation and instability exhibited by high-order polynomial.

B. Antinoise Capability of ESF Center Difference

The target should be a uniform background at the beginning of the deployment. However, with the lack of target field maintenance and low signal-to-noise ratio (SNR) caused by the image, nonuniform noise exists in the imaging background. The ground system MTFC was also recovered to introduce ringing interference. The nonuniformity of the background and the ringing artifacts at the edge of the images is bound to introduce noise in the ESF fitting. This is then substituted into the LSF through the derivation process. The noise error is transferred to the MTF through the FT, and the background noise and ringing artifacts cause inaccuracy in the sharpness assessment results. The JC target with poor background uniformity was imaged using the GF7-BWD PAN band. The noise generated by the target background nonuniformity was analyzed by the SNR of the ESF [23], [30], and its impact on sharpness assessment was measured. The effect of ringing artifacts on the sharpness

assessment was analyzed using GF2-PMS1 images of targets with ringing.

For the JC target, because it is located within the radial target area, the shape of the radial target needs to be considered. Therefore, there is also a visually visible radial dark response in the bright background [see Fig. 10(a), (e), and (i)]. Although the R -square of the fitted curve to the ESF reached 0.99, there was still a large dispersion of the bright target response in the ESF response, such as the right blue dot in Fig. 10(b), (f), and (j). The SNR of the ESF was only 21.15–22.05 dB, substantially smaller than the normal value of 44 dB [25]. The discrete LSF calculated by this low-SNR image derivation shows an abnormal jitter, as indicated by the blue dotted part marked by the arrow in Fig. 10(k), and caused large MTF curves in the sharpness assessment.

The comparison of LSFs obtained from ESFs using center difference and differentiation, and the use of Savitzky–Golay filters for differentiation obtained LSFs, shows that LSFs obtained from center difference are more accurate, such as the smoothed LSFs consisting of green dotted lines in Fig. 10(c), (g), and (k). The blue curve in Fig. 10(d), (h), and (l) is the MTF curve obtained from the LSF directly derived using the ESF and then FT, which has an obvious deviation from the black curve (the average MTF curve of the ACT within one year of the sensor). The red curve is closer to the black curve, which indicates that the center differencing method is effective in improving the accuracy of the MTF after the treatment.

The MTFC processing of the ground system is designed to improve the dynamic MTF of the image and enhance the sharpness of the image. However, there is also the phenomenon of ringing artifacts due to the inaccuracy of the MTF value or the mismatch of the compensation parameter, which leads to overcompensation, as indicated by the red arrows in Fig. 11(a), (b), (d), and (e). The ringing effect was also observed in the edge spread response, as indicated by the red circles in Fig. 11(b), (e), (h), and (k). For the ringing artifacts encountered in the image sharpness assessment, the LSF curves obtained by the commonly used method of direct derivation of the ESF were perturbed, as indicated by the blue dotted line in the red square in Fig. 11(c), (f), (i), and (l). To address this situation, we used the center difference method for the ESF derivation process, which effectively suppresses the perturbation of the LSF curves and ensures smooth LSF curves, such as the red dotted line in Fig. 11(c), (f), (i), and (l).

C. Comparative Analysis of Sharpness Evaluate

An assessment of the existing publications was conducted to validate the results of this study. Currently, there are relatively limited image sharpness assessment studies for the GF1/2/6/7 satellites. In previous studies, we focused on the analysis of MTF (@Nyquist frequency), the results of which are presented in the last row of Table VI. Lu et al. [31] measured the MTF (@Nyquist frequency) of GF1 satellite images over three years using the edge method and obtained an average value of 0.112, with a relative deviation of 7% from the results of the present study. Xu et al. [32] measured the MTF (@Nyquist frequency) and FWHM of the GF2 satellite at a given moment

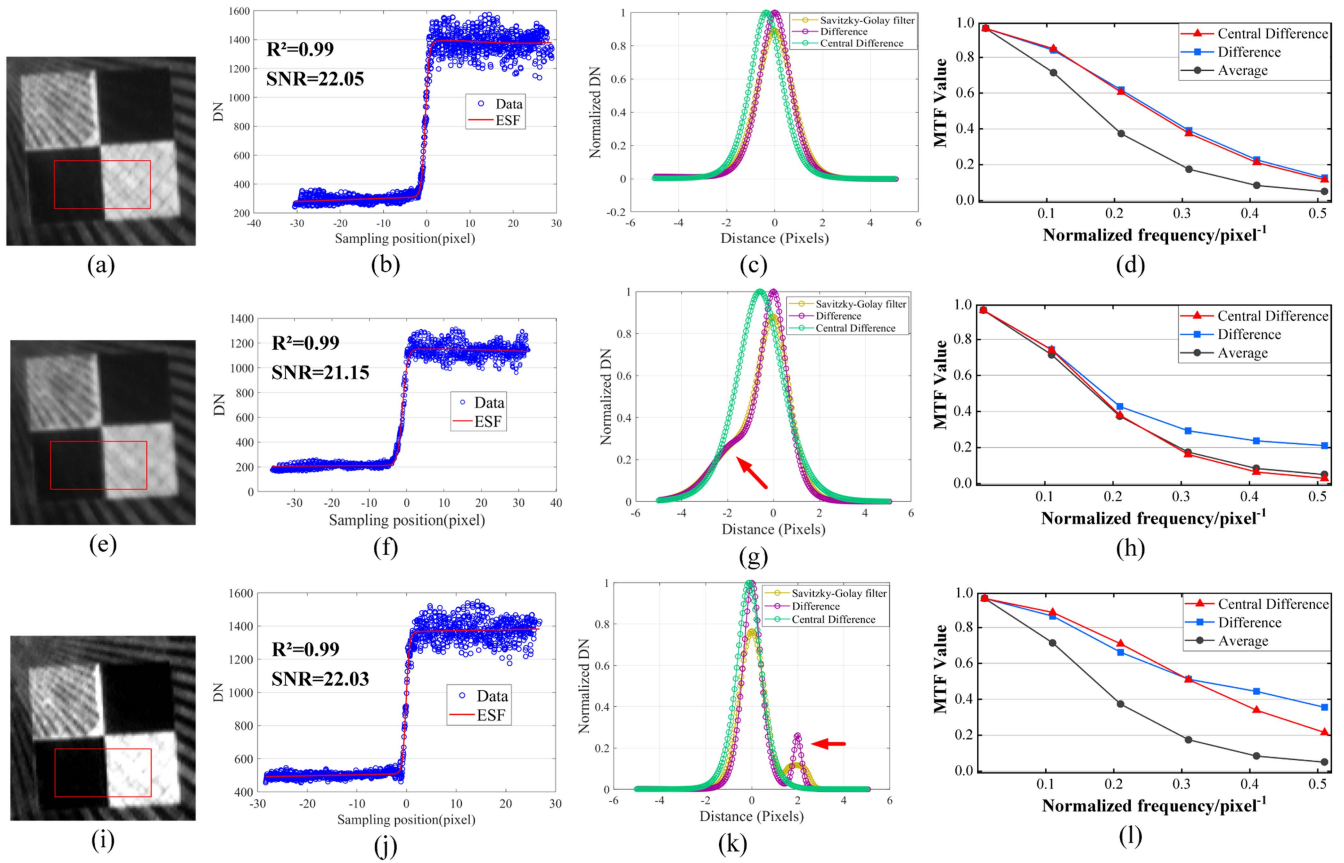


Fig. 10. JC target background noise effects on sharpness assessment. (a) October 2020 target image. (b) ESF fitting. (c) Discrete LSF with different differentiation methods. (d) MTF curve. (e) February 2021 target image. (f) ESF fitting. (g) Discrete LSF with different differentiation methods. (h) MTF curve. (i) June 2021 target image. (j) ESF fitting. (k) Discrete LSF with different differentiation methods. (l) MTF curves.

TABLE VI
GF1/2/6/7 RESULTS OF IMAGE SHARPNESS ASSESSMENT

Satellite	GF1		GF2		GF6	GF7		
	PMS1	PMS2	PMS1	PMS2	PMS	BWD-MUX	BWD-PAN	FWD
RER	0.4786	0.5343	0.4937	0.4995	0.4190	0.5700	0.3208	0.3291
FWHM/pixels	1.2328	1.0795	1.1774	1.1688	1.3923	0.9316	1.8661	1.9521
MTF (@Nyquist frequency)	0.1205	0.1697	0.1323	0.0827	0.0867	0.2364	0.0449	0.0357
MTF (@Nyquist frequency) [25]	0.12	0.17	0.12	0.11	0.07		0.04	0.03

using edge targeting and atmospheric correction techniques, and the results were 0.0998 and 1.5677, respectively. As their study considered atmospheric effects, there are discrepancies with the results of the sharpness assessment in this study. We previously measured the MTF of GF2 using a point-source array method and obtained MTFs (@Nyquist frequency) of 0.0476 and 0.0705 for ALT and ACT, respectively [25]. In this study, the MTFs (@Nyquist frequency) in the ALT and ACT directions, which are similar to the moments in previous point-source method studies, were 0.0582 and 0.0899, respectively. Through these comparisons, the results of this study were in line with those in the existing literature, thus effectively characterizing the sharpness of the GF series remote-sensing satellite images.

We compared the results of this study with international mainstream VLSR images with similar parameters, including IKONOS, QuickBird, WorldView-2, and Pleiades. The FWHM of these images was generally approximately 1.5 pixels, and the MTF (@Nyquist frequency) in the PAN band was mostly in the interval of 0.1–0.2 [21], [33], [34]. The comparison results show that the image sharpness of the Chinese GF series of optical remote-sensing satellites is comparable to that of the same category.

D. Solar Angle and Sharpness Variations

In MTF studies, the magnitude of the sensor's incident radiance has a limited effect on its MTF value [35]. It raises the

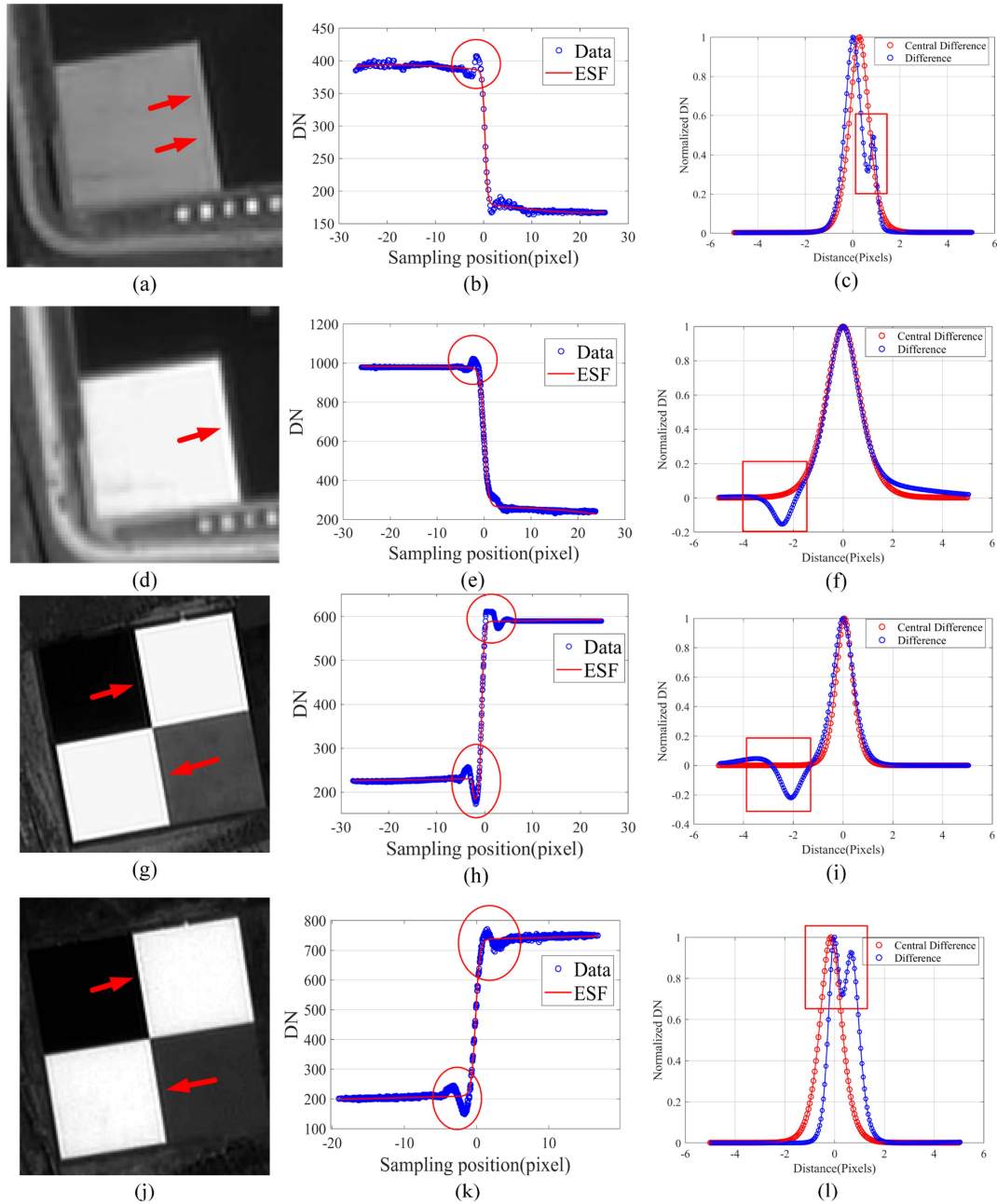


Fig. 11. Target image ringing artifacts sharpness assessment. (a) January 2015 Songshan target image. (b) ESF fitting. (c) LSF obtained by different methods. (d) May 2015 Songshan target image. (e) ESF fitting. (f) LSF obtained by different methods. (g) July 2017 Baotou target image. (h) ESF fitting. (i) LSF obtained by different methods. (j) August 2020 Baotou target image. (k) ESF fitting. (l) LSF obtained by different methods.

question: does image sharpness follow the same law? In this section, the variation of image sharpness under different lighting conditions is discussed by establishing the relationship between image sharpness and solar angle. The relationship between solar zenith angle and image sharpness is experimentally analyzed for three sensors, as shown in Fig. 12(a)–(c) for the GF1-PMS2 sensor, (d)–(f) for the GF2-PMS1 sensor, and (g)–(i) for the GF6-PMS sensor. Observation of the plots did not reveal a trend in the sharpness assessment metrics with solar zenith angle, confirming that solar angle may not affect image sharpness.

VI. CONCLUSION

In this article, a ten-year-long sharpness evaluation of the optical remote-sensing image products GF1/2/6/7 was performed. The magnitude and long-period variations of the RER, FWHM, and MTF (@Nyquist frequency) of the GF images were analyzed based on a fixed-edge target on the ground and compared with similar optical remote-sensing satellites.

- 1) The two GF1/2 sensors exhibited good edge- and frequency-domain responsiveness. The combined RER and MTF (@Nyquist frequency) of the PMS1 and PMS2

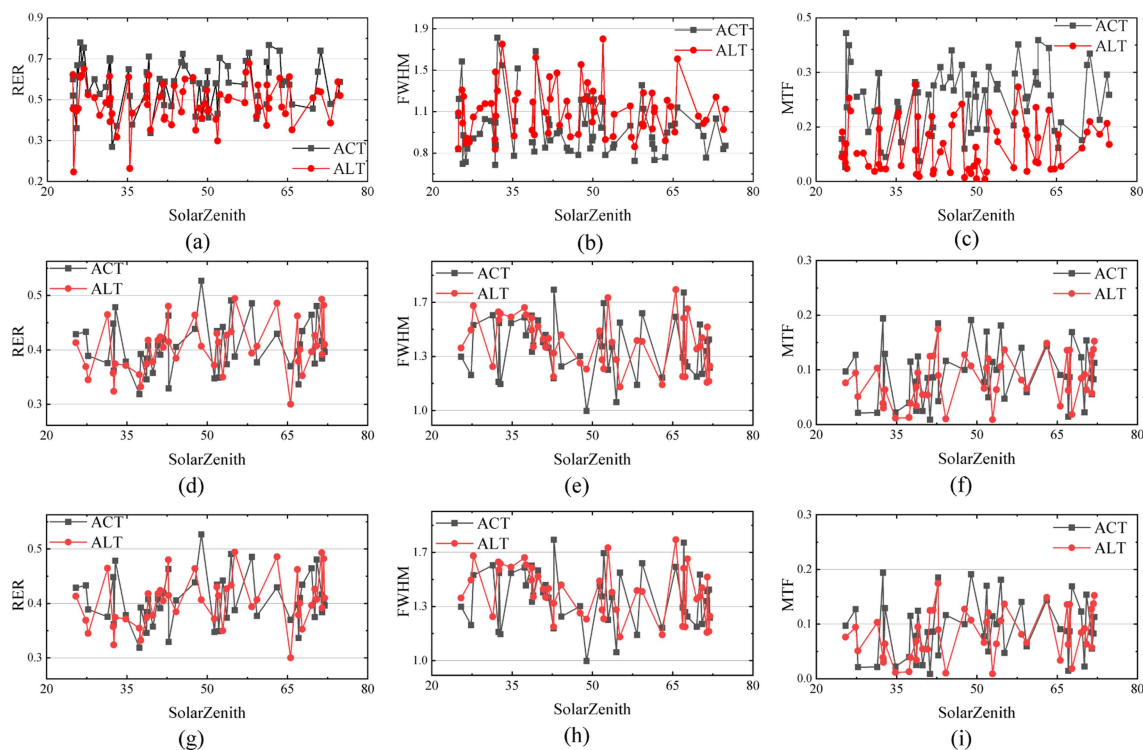


Fig. 12. Relationship between solar zenith angle and sharpness assessment. (a) RER of GF1-PMS2. (b) FWHM of GF1-PMS2. (c) MTF of GF1-PMS2. (d) RER of GF2-PMS1. (e) FWHM of GF2-PMS1. (f) MTF of GF2-PMS1. (g) RER of GF6-PMS. (h) FWHM of GF6-PMS. (i) MTF of GF6-PMS.

sensors of GF1 satellites were 0.48 and 0.53, and 0.12 and 0.17, respectively, the image edge and frequency-domain responsiveness was good, and the FWHM was 1.23 and 1.08, respectively. The image showed a sharpening effect, with a slight difference in the sharpness of the two sensors, and the ACT sharpness was better than the ALT. The fluctuation amplitude of the FWHM of PMS2 was larger, with an SD of 0.44, and more than 46% of the points in the temporal modeling of the evaluation results were within the 95% confidence band. The sharpness exhibited a change of increasing, then oscillating, and then decreasing. The GF2 satellites and the PMS1 and PMS2 sensors have a composite RER and MTF (@ Nyquist frequency), which were 0.50 and 0.50, and 0.08 and 0.09, respectively, and the FWHM was 1.18 and 1.17, respectively. The imaging sharpness of the two sensors was consistent, and the sharpness of the sensors decreased more than that of the ACT in the ALT. More than 43% of the points in the time-series modeling of the evaluation results were within the 95% confidence bands, and the sharpness first increased and then decreased.

- 2) GF6 improved the image sharpening effect compared with GF1/2, but the edge and high-frequency detail responsiveness were reduced. The RER, MTF (@Nyquist frequency), and FWHM of GF6 were 0.42, 0.09, and 1.39, respectively, which improved the image sharpening effect compared with those of GF1/2. However, they also reduced the edge and high-frequency detail responsiveness. The sharpness difference between ACT and ALT was the

smallest for four satellites, and the sensor imaging was stable; more than 48% of the points in the time-series modeling of the evaluation results were within the 95% confidence bands, and the sharpness showed a smooth trend of variation.

- 3) GF7s MS images have good sharpness and show notable sharpening, whereas PAN images require further performance optimization. The RER, MTF (@Nyquist frequency), and FWHM of the PAN images of GF7 are BWD-PAN 0.32, 0.04, and 1.87, and FWD 0.33, 0.04, and 1.95, and all of them indicate that the PAN images have a certain degree of blurring. The MS image sharpness assessment was 0.57, 0.24, and 0.93, respectively, indicating that the MS image exhibited good sharpness and a certain level of sharpening. The image sharpness assessment of ACT was better than that of ALT, and the performance was most evident in the FWD images. Although the GF7 satellite has a shorter time in orbit, more than 60% of the points in the time-series modeling of the assessment results were within the 95% confidence band, and the trend of the change in sharpness was unclear.

In summary, the presence of background noise and ringing artifacts in the target area adversely impacted the sharpness assessment. To address this, the center difference method was introduced for calculating the LSF, which markedly enhanced the precision of sharpness evaluation. An exhaustive analysis of approximately a decade's worth of ground target image data used in this study offers invaluable insights into the long-term performance trends of these satellites. Our research underscores

the efficacy of integrating multiple sharpness metrics for a holistic assessment and uncovers periodic fluctuations in image sharpness over time. The assessment results indicate that, during their on-orbit operations, the GF series satellites consistently maintained high spatial sharpness and stable imaging quality. Furthermore, a horizontal comparison of analogous satellites reveals that China's GF series optical remote-sensing satellites have comparable image sharpness levels.

ACKNOWLEDGMENT

The authors would like to thank the research team for providing the GF images and the reviewers for their helpful comments.

REFERENCES

- [1] D. Poli, F. Remondino, E. Angiuli, and G. Agugiaro, "Radiometric and geometric evaluation of GeoEye-1, WorldView-2 and Pleiades-1A stereo images for 3D information extraction," *ISPRS J. Photogramm. Remote Sens.*, vol. 100, pp. 35–47, Feb. 2015, doi: [10.1016/j.isprsjprs.2014.04.007](https://doi.org/10.1016/j.isprsjprs.2014.04.007).
- [2] *ISO 12233:2023 Photography—Electronic Still Picture Imaging—Resolution and Spatial Frequency Responses*, Accessed: Jun. 15, 2024. [Online]. Available: <https://www.iso.org/standard/79169.html>
- [3] A. Valenzuela, K. Reinke, and S. Jones, "A new metric for the assessment of spatial resolution in satellite imagers," *Int. J. Appl. Earth Observ. Geoinf.*, vol. 114, Nov. 2022, Art. no. 103051, doi: [10.1016/j.jag.2022.103051](https://doi.org/10.1016/j.jag.2022.103051).
- [4] A. C. Bergstrom, D. Conran, and D. W. Messinger, "Gaussian blur and relative edge response," 2023, *arXiv: arXiv:2301.00856*, doi: [10.48550/arXiv.2301.00856](https://doi.org/10.48550/arXiv.2301.00856).
- [5] S. Blonski, K. Ross, M. Pagnutti, and S. Thomas, "Spatial resolution characterization for aerial digital imagery," in *Proc. JACIE Civil Commercial Imag. Eval. Workshop*, Laurel, MD, USA, 2006. [Online]. Available: <https://ntrs.nasa.gov/citations/20060019120>
- [6] T. Igarashi, "ALOS mission requirement and sensor specifications," *Adv. Space Res.*, vol. 28, no. 1, pp. 127–131, Jan. 2001, doi: [10.1016/S0273-1177\(01\)00316-7](https://doi.org/10.1016/S0273-1177(01)00316-7).
- [7] F. Rojas, R. A. Schowengerdt, and S. F. Biggar, "Early results on the characterization of the Terra MODIS spatial response," *Remote Sens. Environ.*, vol. 83, no. 1/2, pp. 50–61, Nov. 2002, doi: [10.1016/S0034-4257\(02\)00086-X](https://doi.org/10.1016/S0034-4257(02)00086-X).
- [8] R. Ryan, B. Baldridge, R. A. Schowengerdt, T. Choi, D. L. Helder, and S. Blonski, "IKONOS spatial resolution and image interpretability characterization," *Remote Sens. Environ.*, vol. 88, no. 1, pp. 37–52, Nov. 2003, doi: [10.1016/j.rse.2003.07.006](https://doi.org/10.1016/j.rse.2003.07.006).
- [9] M. K. Rangaswamy, "Quickbird II: Two-dimensional on-orbit modulation transfer function analysis using convex mirror array—ProQuest," South Dakota State Univ., Brookings, SD, USA, 2003, Accessed: Jul. 18, 2024. [Online]. Available: <https://www.proquest.com/openview/8852e742ebe022441d60ac21092968e6/1?pq-origsite=gscholar&cbl=18750&diss=y>
- [10] D. Leger, F. Viallefont, E. Hillairet, and A. Meygret, "In-flight refocusing and MTF assessment of SPOT5 HRG and HRS cameras," in *Proc. Sensors, Syst., Next-Gener. Satellites VI*, 2003, pp. 224–231, doi: [10.1117/12.462639](https://doi.org/10.1117/12.462639).
- [11] B. Markham, "The Landsat sensors' spatial responses," *IEEE Trans. Geosci. Remote Sens.*, vol. GE-23, no. 6, pp. 864–875, Nov. 1985, doi: [10.1109/TGRS.1985.289472](https://doi.org/10.1109/TGRS.1985.289472).
- [12] J. C. Leachtenauer, W. Malila, J. Irvine, L. Colburn, and N. Salvaggio, "General image-quality equation: GIQE," *Appl. Opt.*, vol. 36, no. 32, Nov. 1997, Art. no. 8322, doi: [10.1364/AO.36.008322](https://doi.org/10.1364/AO.36.008322).
- [13] R. E. Ryan, M. Pagnutti, S. Blonski, K. W. Ross, and T. Stnaley, "High spatial resolution commercial satellite imaging product characterization," Aug. 25, 2005, Accessed: Jul. 18, 2024. [Online]. Available: <https://ntrs.nasa.gov/citations/20050238456>
- [14] S. Saunier et al., "Coordinating and monitoring quality information for the Copernicus Services: Case study with optical data abstract uFFFFD," *IEEE Geosci. Remote Sens. Mag.*, vol. 3, no. 2, pp. 24–40, Jun. 2015, doi: [10.1109/MGRS.2015.2439394](https://doi.org/10.1109/MGRS.2015.2439394).
- [15] D. Helde, J. Choi, and C. Anderson, "On-orbit modulation transfer function (MTF) measurements for IKONOS and QuickBird," Jan. 2007, Accessed: Jun. 15, 2024. [Online]. Available: <https://ntrs.nasa.gov/citations/20070038252>
- [16] D. Helder, T. Choi, and M. Rangaswamy, "Quickbird satellite in-orbit modulation transfer function (MTF) measurement using edge, pulse and impulse methods for summer 2003," Aug. 1, 2005, Accessed: Jul. 18, 2024. [Online]. Available: <https://ntrs.nasa.gov/citations/20050214545>
- [17] K. Jacobsen, H. Topan, A. Cam, M. Özendi, and M. Oruc, "Radiometric and geometric characteristics of Pleiades images," *Int. Arch. Photogramm. Remote Sens. Spatial Inf. Sci.*, vol. XL-1, pp. 173–177, Nov. 2014, doi: [10.5194/isprsarchives-XL-1-173-2014](https://doi.org/10.5194/isprsarchives-XL-1-173-2014).
- [18] M. Crespi and L. De Vendictis, "A procedure for high resolution satellite imagery quality assessment," *Sensors*, vol. 9, no. 5, pp. 3289–3313, May 2009, doi: [10.3390/s90503289](https://doi.org/10.3390/s90503289).
- [19] V. Pampanoni, F. Fascetti, L. Cenci, G. Laneve, C. Santella, and V. Boccia, "Analysing the relationship between spatial resolution, sharpness and signal-to-noise ratio of very high resolution satellite imagery using an automatic edge method," *Remote Sens.*, vol. 16, no. 6, 2024, Art. no. 1041, doi: [10.3390/rs16061041](https://doi.org/10.3390/rs16061041).
- [20] J. C. Vrabel et al., "System characterization report on the Satellogic NewSat multispectral sensor," U.S. Geological Survey, 2021-1030-L, 2022, doi: [10.3133/ofr20211030L](https://doi.org/10.3133/ofr20211030L).
- [21] S. J. Cantrell et al., "System characterization report on the Pleiades Neo Imager," Open-File Rep. 2021-1030, 2023. [Online]. Available: <https://www.usgs.gov/publications/system-characterization-report-pleiades-neo-imager>
- [22] L. Cenci, V. Pampanoni, G. Laneve, C. Santella, and V. Boccia, "Presenting a semi-automatic, statistically-based approach to assess the sharpness level of optical images from natural targets via the edge method—Case study: The Landsat 8 OLI-L1T data," *Remote Sens.*, vol. 13, no. 8, Jan. 2021, Art. no. 1593, doi: [10.3390/rs13081593](https://doi.org/10.3390/rs13081593).
- [23] R. Eon et al., "Landsat 9 thermal Infrared sensor-2 (TIRS-2) pre- and post-launch spatial response performance," *Remote Sens.*, vol. 16, no. 6, Jan. 2024, Art. no. 1065, doi: [10.3390/rs16061065](https://doi.org/10.3390/rs16061065).
- [24] Y. Wang, W. Yi, Y. Zeng, W. Su, and W. Qi, "Assessment of image sharpness evaluation methods and image sharpness changes in GF-4 satellite time-series data," in *Proc. 13th Int. Conf. Graph. Image Process.*, 2022, vol. 12083, Art. no. 127, doi: [10.1117/12.2623537](https://doi.org/10.1117/12.2623537).
- [25] L. Li, Y. Jiang, X. Shen, and D. Li, "Long-term assessment and analysis of the radiometric quality of standard data products for Chinese Gaofen-1/2/6/7 optical remote sensing satellites," *Remote Sens. Environ.*, vol. 308, Jul. 2024, Art. no. 114169, doi: [10.1016/j.rse.2024.114169](https://doi.org/10.1016/j.rse.2024.114169).
- [26] S. Kerr, "Recommendations for the detection and analysis of the ISO 12233:2023 e-SFR slanted star," *Electron. Imag.*, vol. 36, no. 9, pp. 271–1–271–6, Jan. 2024, doi: [10.2352/EL.2024.36.9.IQSP-271](https://doi.org/10.2352/EL.2024.36.9.IQSP-271).
- [27] N. Markevich and I. Gertner, "Comparison among methods for calculating FWHM," *Nucl. Instrum. Methods Phys. Res. Sect. A, Accelerators, Spectrometers, Detectors Assoc. Equip.*, vol. 283, no. 1, pp. 72–77, Oct. 1989, doi: [10.1016/0168-9002\(89\)91258-8](https://doi.org/10.1016/0168-9002(89)91258-8).
- [28] A. Q. Valenzuela and J. C. G. Reyes, "Comparative study of the different versions of the general image quality equation," *ISPRS Ann. Photogramm. Remote Sens. Spat. Inf. Sci.*, vol. IV-2/W5, pp. 493–500, May 2019, doi: [10.5194/isprs-annals-IV-2-W5-493-2019](https://doi.org/10.5194/isprs-annals-IV-2-W5-493-2019).
- [29] L. Chen et al., "An introduction to the Chinese high-resolution Earth observation system: Gaofen-1~7 civilian satellites," *J. Remote Sens.*, vol. 2022, Apr. 2022, Art. no. 9769536, doi: [10.34133/2022/9769536](https://doi.org/10.34133/2022/9769536).
- [30] H. Hwang, Y.-W. Choi, S. Kwak, M. Kim, and W. Park, "MTF assessment of high resolution satellite images using ISO 12233 slanted-edge method," in *Proc. Image Signal Process. Remote Sens. XIV*, 2008, pp. 34–42, doi: [10.1117/12.800055](https://doi.org/10.1117/12.800055).
- [31] C. Lu, Q. Yu, and Y. Yuan, "GaoFen-1 performance and status after nine years on orbit," in *Proc. 7th Int. Symp. Space Opt. Instrum. Appl.*, 2023, pp. 20–29, doi: [10.1007/978-981-99-4098-1_3](https://doi.org/10.1007/978-981-99-4098-1_3).
- [32] W. Xu, X. Long, and Q. Li, "Evaluation of the radiometric quality of images from the Gaofen-2 satellite camera," *Space Return Remote Sens.*, vol. 36, no. 4, pp. 1–9, 2015, doi: [10.3969/j.issn.1009-8518.2015.04.001](https://doi.org/10.3969/j.issn.1009-8518.2015.04.001).
- [33] Á. Q. Valenzuela and J. C. G. Reyes, "Basic spatial resolution metrics for satellite imagers," *IEEE Sensors J.*, vol. 19, no. 13, pp. 4914–4922, Jul. 2019, doi: [10.1109/JSEN.2019.2902512](https://doi.org/10.1109/JSEN.2019.2902512).
- [34] A. Meygret, G. Blanchet, C. Latry, A. Kelbert, and L. Gross-Colzy, "On-orbit star-based calibration and modulation transfer function measurements for PLEIADES high-resolution optical sensors," *IEEE Trans. Geosci. Remote Sens.*, vol. 57, no. 8, pp. 5525–5534, Aug. 2019, doi: [10.1109/TGRS.2019.2900026](https://doi.org/10.1109/TGRS.2019.2900026).

- [35] S. Horiuchi, S. Yoshida, and M. Yamamoto, "Simulation of modulation transfer function using a rendering method," *Opt. Exp.*, vol. 21, no. 6, Mar. 2013, Art. no. 7373, doi: [10.1364/OE.21.007373](https://doi.org/10.1364/OE.21.007373).



Jiayang Cao received the B.S. degree in geomatics engineering from the Institute of Disaster Prevention, Langfang, China, in 2022. He is currently working toward the M.S. degree in geography with the College of Urban and Environmental Sciences, Hubei Normal University, Huangshi, China.

His research direction is remote sensing radiometric calibration and quality assessment.



Litaο Li was born in 1988. He received the Ph.D. degree in photogrammetry and remote sensing from the State Key Laboratory for Information Engineering in Surveying, Mapping and Remote Sensing, Wuhan University, Wuhan, China, in 2019.

Since 2019, he has been with the College of Urban and Environmental Sciences, Hubei Normal University, Huangshi, China, where he became an Associate Professor in 2023. His research interests include radiometric calibration and processing of spaceborne optical imagery.



Yonghua Jiang received the B.S. and Ph.D. degrees in remote sensing science and technique from the School of Remote Sensing and Information Engineering, Wuhan University, Wuhan, China, in 2010 and 2015, respectively.

Since 2015, he has been with the School of Remote Sensing and Information Engineering, Wuhan University, where he became a Professor in 2023. His research interests include the geometry processing of spaceborne optical imagery.



Xin Shen received the B.Sc. degree in information engineering, the M.Sc. degree in cartography and geographic information systems, and the Ph.D. degree in photogrammetry and remote sensing from Wuhan University, Wuhan, China, in 2003, 2006, and 2012, respectively.

He is currently an Associate Professor with LIES-MARS, Wuhan University. His research interests include satellite mission planning and evolutionary computation in remote sensing applications.



Deren Li received the Ph.D. degree in photogrammetry and remote sensing from the University of Stuttgart, Stuttgart, Germany, in 1985, and the Honorary Doctorate degree in photogrammetry and remote sensing from ETHZürich, Zürich, Switzerland, in 2008.

He is currently a Scientist in surveying, mapping, and remote sensing with Wuhan University, Wuhan, China. He enjoys dual memberships of both Chinese Academy of Sciences and the Chinese Academy of Engineering. He is also a member of the International

Eurasia Academy of Sciences and the International Academy of Astronautics. International Society for Photogrammetry and Remote Sensing awarded him the Honorary Member and the Brock Gold Medal in recognition of outstanding contributions to photogrammetry.



Meilin Tan received the B.S. degree in remote sensing science and technology and the M.S. degree in surveying and mapping engineering from Wuhan University, Wuhan, China, in 2010 and 2018, respectively.

He is currently an Engineer with Inner Mongolia Autonomous Region Surveying and Mapping Geographic Information Center, Hohhot, China.